Advanced Powder Technology 33 (2022) 103862

Contents lists available at ScienceDirect

Advanced Powder Technology

journal homepage: www.elsevier.com/locate/apt

Nanoarchitectonics of Ag-modified g-C_3N_4@halloysite nanotubes by a green method for enhanced photocatalytic efficiency

Hoa T. Nguyen [a], Huan V. Doan [a,b], T. Thanh-Bao Nguyen [c], Xuan N. Pham [a,*]

[a] Department of Chemical Engineering, Hanoi University of Mining and Geology, 18 Pho Vien, Duc Thang, Bac Tu Liem, Hanoi, Viet Nam
[b] School of Chemistry, University of Bristol, Bristol BS8 1TS, UK
[c] Institute of Physics, Vietnam Academy of Science and Technology, 18C Hoang Quoc Viet, Hanoi, Viet Nam

ARTICLE INFO

Article history:
Received 7 July 2022
Received in revised form 18 September 2022
Accepted 23 October 2022

Keywords:
Ag-g-C_3N_4
Ag-g-C_3N_4@HNTs
HNTs
Tetracycline
Photocatalyst

ABSTRACT

In this study, a facile and cost effective green synthesis has been utilized for the synthesis of silver nanoparticles (Ag-NPs)–modified graphitic carbon nitride (Ag-g-C_3N_4) and halloysite nanotubes (HNTs) using *Centella Asiatica* (L.) extract, urea and mineral source of natural halloysite (HNTs), respectively. Here, silver ions (Ag^+) were reduced to Ag-NPs using an aqueous *Centella Asiatica* (L.) as reducing and capping agent. The synthesized Ag-g-C_3N_4@HNTs were characterized by various physiochemical methods such as XRD, FT-IR, BET, SEM, TEM, EDS–mapping, UV–vis-DRS, PL, XPS and EPR methods. In the photocatalytic experiment, Ag-g-C_3N_4@HNTs nanocomposite with silver surface plasmon resonance of Ag-NPs and multi-layer hollow nanotubes was outperformed by the individual components. With an in-depth study on the photocatalytic mechanisms, we can conclude that the enhanced performance of the nanocomposite is due to the effective separation of photogenerated electrons and superoxide radicals ($^{\bullet}O_2^-$) in water molecules. The photocatalyst preserved excellent photostability for up to four cycles (with a minor activity reduction from 95% to 91%). These results demonstrated the development of novel semiconductors from inexpensive resources with effective photoactivity to mitigate environmental problems.

1. Introduction

According to the United Nations World Water Assessment Program (UN WWAP), industries including textile, paper, and pharmaceutical manufacture discharge 300 to 400 million tons of untreated organic pollutants annually, contaminating water [1] and causing significant environmental damage. To overcome this, most countries have carried out strict regulations to control the environment, i.e.. Therefore, many studies have been carried out to find a pragmatic solution to curb water pollution and protect the environment from further damage. As such, photocatalysis, a reaction process onto a catalyst surface under natural sunlight, is considered an effective method and has been employed in the degradation of many polluted organic compounds such as dyes [2], antibiotics [3], analgesics [4], and herbicides [5]. Tetracycline (TC) is one of the most prevalently used compounds in antibiotics. It poses a huge environmental hazard since its abuse can destroy the ecological structure of organisms and represent a severe threat to humans by interrupting the food chain [6]. Degradation of TC thus has immediate and pressing applications to enable a cleaner, more resilient, and productive environment. For this to be effective, next-generation catalysts that enhance photocatalytic efficiency need to be developed.

Nanocarbon materials are interested in many fields because of their unique properies such as chemical stability, good electrical conductivity and high surface area. The carbon semiconductors can accelerate the transfer of electrons from the surface photocatalyst to the liquid–solid separator. In particular, graphite carbon nitride is considered a potential candidate because of its photocatalytic ability and catalyst support ability [7–10]. Graphitic carbon nitride (g-C_3N_4) is a promising photocatalyst due to a mild bandgap of about 2.7 eV. This material has been used in some useful applications such as sensors [11], supercapacitors [12], adsorption [13], organic synthesis [14], and hydrogen evolution [15]. However, this material has disadvantages such as low surface area, weak visible-light absorption, rapid recombination of the electron-hole pairs, and low electron separation yield. Doping g-C_3N_4 with metallic or non-metallic elements is an effective way to improve photocatalytic efficiency in removing pollutants in wastewater [16,17]. For example, sodium-doped g-C_3N_4 (Na-CN) was created by annealing a mixture of sodium hydroxide

* Corresponding author.
E-mail address: phamxuannui@humg.edu.vn (X.N. Pham).

https://doi.org/10.1016/j.apt.2022.103862

and dicyandiamide [18]. Na-CN material can inhibit crystal growth by Na, thus improving the surface area, adjusting the surface area of the valence and conduction band structure, and effectively separating the charge carriers. Under visible light, the photocatalytic performance of Na-CN material was more significant than pure g-C_3N_4 in the degradation of Rhodamine B (RhB). The one-step synthesis of oxygen-doped g-C_3N_4 (x-OCN) by substituting O atoms for N in the g-C_3N_4 structure has also been studied [19]. As shown in this study, the high content of doped-O in the matrix of 40-OCN resulted in narrow bandgap energy and lower recombination rate of photogenerated electrons and holes, thus enhancing visible light photodegradation of Rhodamine B (RhB). Furthermore, the deposition of precious metals on the surface of g-C_3N_4 has received much attention [20]. Gold (Au) [21], platinum (Pt) [22], and ruthenium (Ru) [23] were the first metals used, but Ag has recently gained popularity due to its low cost and ease of synthesis. Ag/g-C_3N_4 has been studied and applied for the degradation of organic pollutants in an aqueous environment as well as in water separation applications [24,25].

Besides, graphitic carbon nitride has been combined with low-cost, non-toxic, and characteristic morphological clay minerals such as bentonites and halloysites (HNTs) as supports to improve catalytic activity in the composite material. For example, bentonite/g-C_3N_4 nanocomposite degrades methylene blue (MB) in wastewater treatment [26]. The resultant material has longer absorption wavelengths (increased to 500 nm from 474 nm in the pure g-C_3N_4) and a higher BET surface area (24.1 m^2/g in bentonite/g-C_3N_4 compared to 5.9 m^2/g in g-C_3N_4), and improved adsorptive activity compared with that of g-C_3N_4. Halloysites (HNTs), a biocompatible and abundant natural aluminosilicate, support the g-C_3N_4-based photocatalyst in effectively separating photogenerated electron-hole pairs [27]. HNTs nanotubes have different surface chemistry on their internal and external surfaces. The internal surface of HNTs is composed of gibbsite octahedral sheet (Al-OH) groups and is positively charged, while its negatively charged outer surface consists of siloxane groups (Si-O-Si) [28]. Because of the strain induced by the lattice mismatch between neighboring silicon dioxide and aluminum oxide sheets, halloysite tubes are rolled into cylinders. The electrostatic contact with the negatively charged halloysite can suppress the charge recombination, which promotes the immigration of electrons and holes. The nanotube structure can help to increase surface area and improve absorption visible-light ability, thus playing a major role in improved photocatalytic performance. For example, a new adsorbent g-C_3N_4-IL@HNT was fabricated and used to extract benzene and phenol contaminants from water samples [29]. The g-C_3N_4-IL@HNT composite showed effective adsorption by multifunctional groups, allowing interaction with pollutants, although the photocatalytic capacity of g-C_3N_4 was not mentioned in this study. 1D mesoporous tubular g-C_3N_4 (TCN) improved photocatalytic degradation efficiency of tetracycline by 4.6 times that of g-C_3N_4 (CN) using halloysite as a hard template through a calcination-leaching method [30]. HNTs were also shown to give TCN a large surface area, more active sites, the ability to use visible light sources, and the ease of separation of charge carriers. As far as we know, there hasn't been any research about Ag-g-C_3N_4@HNTs photocatalyst for TC degradation. Therefore, dispersing Ag-g-C_3N_4 onto HNTs surface offers a viable method to solve the above problem.

Here we report on a green synthesis process from AgNPs–loaded graphitic carbon nitride (Ag-g-C_3N_4) and natural halloysite (HNTs) as a novel semiconductor. The catalytic performance of Ag-g-C_3N_4@HNTs nanocomposite was investigated in the photodegradation of TC as a pollutant. We investigated the effects of various photocatalysts and different photocatalytic dosages on TC degradation efficiency. The reusability and stability of the photocatalysts were evaluated to assess their long-term applicability.

2. Experimental

2.1. Materials

The raw halloysite mineral came from Yenbai Province, Vietnam. Halloysite was treated according to our previous research procedure [31]. The chemical composition of the halloysite was 32.26% SiO_2, 13.67% Al_2O_3, 4.38% Fe_2O_3, 0.39% TiO_2, 2.75% CuO, 1.25% MgO, 22.70% Na_2O, and there was 22.60% loss on ignition (LOI) (wt.%). *Centella Asiatica* (L.) Urban leaves were collected from local sources. The chemical reagents used in this study include urea ($(NH_2)_2CO$), sulphuric acid (H_2SO_4), silver nitrate ($AgNO_3$), and tetracycline (TC), which were supplied by Sigma-Aldrich and used without further purification. All the solutions were prepared with deionized water.

2.2. Synthesis of Ag-g-C_3N_4@HNTs nanocomposite

2.2.1. Synthesis of silver nanoparticles (AgNPs)

Firstly, silver nanoparticles were synthesized using a green method [32]. Briefly, *Centella Asiatica* (L.) were washed with double distilled water and dried naturally at room temperature before being finely ground to powder. 25 g of the powdered plant was extracted by the Soxhlet system with 100 mL of distilled water and ethanol (80:20 v/v ratio). After 4 h, the obtained extract was collected and stored at 4 °C for further experiments.

5% (v/v) of the extract was mixed with 20 mL of 0.01 M silver nitrate solution in an Erlenmeyer flask on the magnetic stirrer (300 rpm, 25 °C and 24 h), and the color of the solution changed from the yellowish-brown to dark-brown designates the formation of colloidal AgNPs.

2.2.2. Synthesis of Ag-g-C_3N_4@HNTs photocatalysts

A schematic procedure of Ag-modified g-C_3N_4@Halloysite nanotubes fabrication is shown in Fig. 1. The g-C_3N_4@HNTs nanocomposite was synthesized by the calcination method. In detail, a mix of 3 g of urea and 0.5 g of HNTs was put into a ceramic crucible with a cover, placed in a muffle furnace and heated at 500 °C at a heating rate of 2 °C. min^{-1} for 1 h and then cooled to room temperature, producing a light-yellow powder.

After the above procedure, 10 mL of the biosynthesized AgNPs using aqueous extract of *Centella Asiatica* (L.) was added into 0.1 g of g-C_3N_4@HNTs composite. The mixture was continuously stirred for 1 h at room temperature. Finally, the Ag-g-C_3N_4@HNTs nanocomposite was washed with DI water, filtered, and dried at 80 °C for 24 h, producing a brown powder.

2.3. Characterizations

The crystal structure of the synthesized samples was determined by X-ray powder diffraction (XRD) using a D8 ADVANCE system (CuKα1 copper radiation, λ = 0.154 nm, 3° min^{-1} scanning speed, Bruker, Germany). Surface morphology was observed by a scanning electron microscope (S–4800, Hitachi). The Fourier transform infrared spectra (FT–IR) were measured with an FTIR Affinity-1S (SHIMADZU). X-ray energy dispersion (EDX) and EDX mapping were performed with a JED–2300 with a gold coating. Transmission electron micrographs were obtained from a JEM-2100F (JEOL, Japan) at 200 kV, with the samples drop cast onto carbon (high purity)-coated copper grids. The UV–vis diffuse reflectance

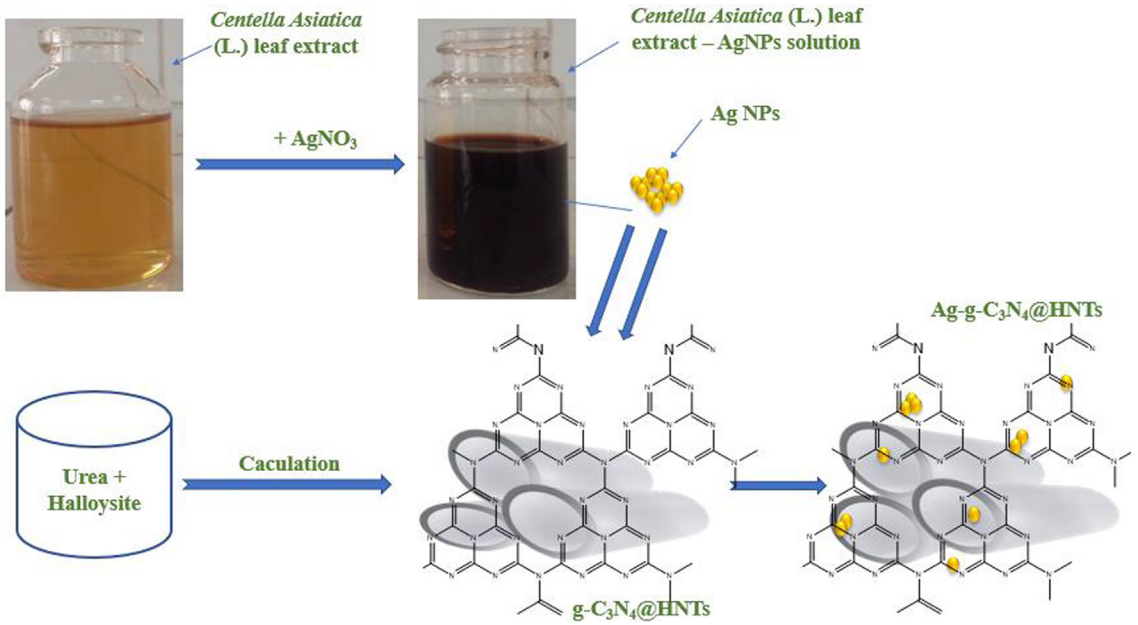

Fig. 1. Schematic representation illustrating the fabrication of Ag-modified g-C_3N_4@Halloysite nanotubes.

(DRS–UV) and photoluminescence (PL) spectra were recorded with the UV–2600 spectrophotometer (Varian), respectively. The Brunauer–Emmett–Teller (BET) specific surface area was determined at liquid–nitrogen temperature (77 K) using the N2 adsorption–desorption technique on a ChemBET–3030 system. Also, X-ray photoelectron spectroscopy (XPS) was conducted using an ESCALab 250 spectrometer (Thermo VG, UK). Photocurrent analyses were performed on an electrochemical analyzer (CHI660B Instrument) in a standard three-electrode system, with Ag/AgCl and a saturated calomel electrode used as a counter electrode and a reference electrode, respectively. Electron paramagnetic resonance (EPR) measurements were carried out on a Bruker ESP 500 spectrometer.

2.4. Performances of photocatalytic activity

The photocatalytic activity of the materials was evaluated using TC in an aqueous solution with irradiation by a 125 W Xe lamp at room temperature. In the experiment, 50 mg of the photocatalysts were dispersed in the TC solution (30 mL, 50 ppm). Before irradiation, the mixture was magnetically stirred for 30 min to achieve the adsorption–desorption equilibrium. Initial concentration (*Co*) was taken at this point. After each hour, 3 mL of the suspension was taken out and then filtrated to remove the catalysts. The concentration of the tetracycline (*C*) was analyzed using a UV–vis 2450 spectrometer, and the TC degradation was calculated using the following Eq. (1):

$$\text{TC degradation } (\%) = \frac{C_o - C}{C_o} \text{ x } 100\% \quad (1)$$

where Co (ppm) is the initial concentration and C (ppm) is the calculated concentration of TC in the mixture taken from the reaction after 1–4 h.

The effect of four different reagents on the photocatalytic degradation reaction was investigated, in which *tert*-Butyl alcohol (TBA), potassium dichromate ($K_2Cr_2O_7$), ammonium oxalate monohydrate (AO), and 1.4-benzoquinone (BQ) of 10^{-6} mol L^{-1} were used as capture reagents for the hydroxyl radicals (•OH), electrons (e^-), holes (h^+), and superoxide radicals ($^{\bullet}O_2^-$) in the photocatalytic degradation reaction of TC. Scavengers were added to the TC solution (50 ppm) containing 50 mg of Ag-g-C_3N_4@HNTs. The mixed solution was stirred at 300 rpm in the dark for 30 min before irradiation. About 3 mL of the suspension was taken out after each hour and then filtrated to remove the catalyst. Samples were analyzed using a UV–vis 2450 spectrometer at maximum wavelength λ = 357 nm.

3. Results and discussion

3.1. Structural properties

Crystal and chemical structures of the synthesized materials, including g-C3N4, HNTs, and g- C_3N_4/HNTs, Ag-g-C_3N_4@HNTs nanocomposites, were analyzed using powder X-ray diffraction (PXRD) and Fourier-transform infrared (FT-IR) spectroscopy. The results are shown in Fig. 2.

Fig. 2(a) shows that g-C_3N_4 exhibited two main characteristic diffraction peaks at 27.3° and 13.2°, corresponding to the hexagonal phase of polymeric g-C_3N_4 (JCPDS 87–1526) [33]. The strong peak of g-C_3N_4 at 27.3° can be indicated as the (002) plane of g-C_3N_4, which reflects the interlayer stacking of the aromatic system. The weak peak of g-C_3N_4 at about 13.2° can be indexed as (100) planes of g-C_3N_4, which reflect the in-planar-s-triazine structural packing motif composed of the tris-s-triazine units [34]. For the pure halloysite, seven main peaks at 12.2°, 19.9°, 24.84°, 35.02°, 37.98°, 54.5° and 62.6° can be observed, corresponding to the (001), (100), (002), (110), (003), (210) and (300) diffraction planes, respectively [35]. Notably, the pure HNTs exhibit a sharp peak of diffraction (2θ) at 12.2°, corresponding to a spacing (d) between diffracting planes of 7.35Å, indicating that the HNTs in this study is in the dehydrated form [36], with diffraction (2θ) at 24.84°, corresponding to the dehydrated state of the (002) basal reflection, (d) of 3.58Å, and the (110) basal reflection at 2θ = 19.9° with d = 4.73Å [37]. Remarkably, the main primary of HNTs and g-C_3N_4 can be found in the nanocomposite sample, implying that the structure of both HNTs and g-C_3N_4 is preserved in the nanocomposite. In the Ag-g-C_3N_4@HNTs composite, the crystalline of AgNPs was observed at 2θ = 32.2° and 46.2°, corresponding to the (111) and

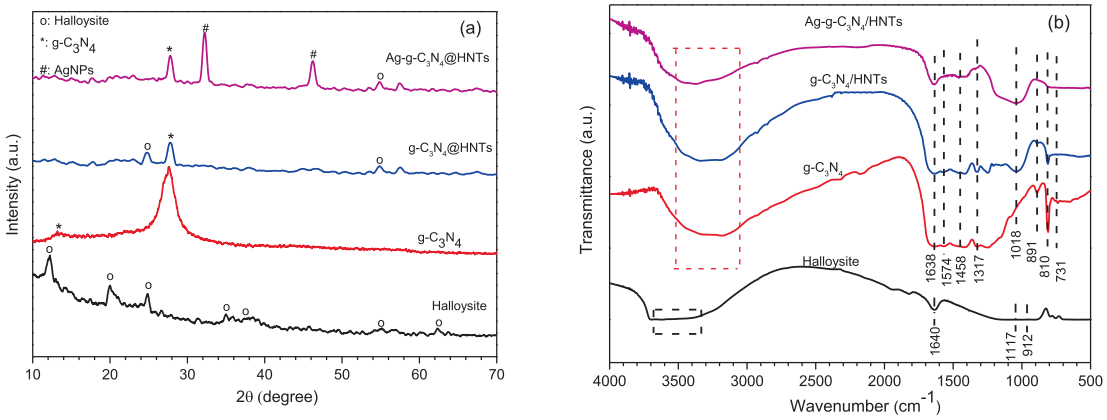

Fig. 2. (a) XRD patterns of g-C_3N_4, HNTs, g-C_3N_4@HNTs, and Ag-g-C_3N_4@HNTs, (b) FT-IR spectra of g-C_3N_4, HNTs, g-C_3N_4@HNTs, and Ag-g-C_3N_4@HNTs.

(200) diffraction planes, respectively. The Ag-NPs peaks indicate the crystalline silver face-centered-cubic (FCC) phase [38].

Fig. 2(b) shows the FT-IR spectra of halloysite and g-C_3N_4, and the spectrum of pure halloysite exhibited the characteristic absorption peaks at 3600, 1640, 1033–1117, 912 cm^{-1}. The absorption band range from 3300 to 3700 cm^{-1} is assigned to the O—H vibrations of the Al-OH at the inner surface [39]. The Si-O stretching vibration bands correspond to the range from 1033 to 1117 cm^{-1}. The O—H deformation vibration of the internal Al-OH groups corresponds to the band at 912 cm^{-1}. The absorbed water on HNTs corresponds to deformation vibration at 1640 cm^{-1} [40]. The peaks at 1238, 1317, and 1458 cm^{-1} in the g-C_3N_4 sample could be attributed to aromatic C—N [41], whereas the peaks at 1574 and 1638 cm^{-1} may be assigned to the presence of C=N bonds [41]. Furthermore, the peaks that appeared at 810 and 891 cm^{-1} could be attributed to the characteristic breathing vibration bands of the C—N heterocycle [42]. The broad peak at 3100–3300 cm^{-1} corresponds to the stretching vibration modes of the –NH and the adsorbed water molecules [43]. All chemical bonds of HNTs and g-C_3N_4 were preserved in the nanocomposite materials.

The elemental valence state of the sample was determined by XPS, and the result is shown in Fig. 3. The survey spectra (Fig. 3 (a)) indicated that C, N, Ag were found on the Ag-g-C_3N_4@HNTs nanocomposite surface. According to the high-resolution spectrum of C 1s (Fig. 3(b)), the binding energies at 284.9 eV might be assigned to the C—C coordination of the surface graphitic carbon. In contrast, the binding energies at 288.3 eV correspond to N=C—N in CN units, and the binding energies at 289.6 eV could be ascribed to the C atoms bonded with O (C—O) [44,45]. The binding energies of N 1s (Fig. 3(c)) show four peaks at 398.7, 399.5, 400.2 and 401.2 eV, which could be assigned to the pyridine N, pyrrolic N, graphitic N, and amino-functional group, respectively [46,47]. In addition, the high-resolution spectrum of Ag 3d (Fig. 2d) was observed at 368.1 eV and 374.1 eV, with the 3d bimodal splitting at 6 eV, corresponding to the metallic Ag^o [48]. These results again confirmed that the silver was successfully loaded into the electronic structure of g-C_3N_4 and the formation of Ag-g-C_3N_4 on the surface of the halloysite nanotubes.

3.2. Textural properties

SEM, TEM, and SAED were examined to analyze the structural and morphological characteristics of g-C_3N_4, pure HNTs, and Ag-g-C_3N_4@HNTs photocatalyst (Fig. 4). Fig. 4(a,d) show that g-C_3N_4 has a nanosheet structure similar to graphene. The TEM images of pure HNTs clearly show the hollow tubular diameter of 20–40 nm and length of 400 nm to 750 nm (Fig. 4(b,e)). This result could be explained by the fact that HNTs are composed of siloxane (Si-O-Si) and luminol (Al-OH) groups, with the existence of certain Al-OH and Si-OH groups at the edges of the material or as structural faults causing halloysite tubes to be rolled into cylinders [49]. Fig. 3f showed a TEM image of Ag-g-C_3N_4@HNTs nanocomposite with a large amount of black dots corresponding to Ag NPs that were dispersed into g-C_3N_4 nanosheets. Ag nanoparticles have diameters ranging from 5 to 20 nm. The multi-layer hollow tube structure, as seen in the Ag-g-C_3N_4@HNTs nanocomposite (Fig. 3c), is due to the integration of exfoliated graphitic carbon nitride nanosheets [46] into the halloysite. The crystalline of g-C_3N_4 can be seen in the dotted pattern of the selected area diffraction SAED pattern (Fig. 4 (g,h,k).

The compositional analysis of Ag-g-C_3N_4@HNTs was conducted by EDX measurements (Fig. 5). As shown in Fig. 5, the Ag-g-C_3N_4@HNTs nanocomposite revealed the presence of C, N, O, Al, Si, and Ag elements, which correspond to the different positions of 0.2, 0.4, 0.5, 1.5, 1.8 and 2.0 keV, respectively.

Fig. 6 displays the N_2 adsorption–desorption isotherms of the HNTs, g-C_3N_4, and Ag-g-C_3N_4@HNTs nanocomposite samples and the corresponding pore size distribution. According to the IUPAC classification, these three adsorption–desorption isotherms have typical IV profiles with distinct hysteresis loops of Type H4 (Fig. 6(a), demonstrating the predominant mesoporous character of these three materials. As shown in Table 1, the BET surface area, pore-volume, and average pore diameter of HNTs are 28.01 m^2/g, 0.137 $cm^3\ g^{-1}$, and 19.76 nm, respectively. The BET surface area, pore-volume, and average pore diameter of the g-C_3N_4 nanosheet are 20.12 m^2/g, 0.107 $cm^3\ g^{-1}$, and 20.34 nm, respectively. Meanwhile, the BET surface, pore-volume, and pore size of the Ag-g-C_3N_4@HNTs nanocomposite were considerably higher than the pure halloysite and g-C_3N_4, with values of 43.04 m^2g^{-1}, 0.273 cm^3g^{-1}, and 28.14 nm, respectively. This demonstrate that the larger mesopores was formed on the fabrication of nanocomposite. As a result, Ag-g-C_3N_4@HNTs nanocomposite promises to be a material with far superior light absorption ability and photocatalytic activity than halloysite and g-C_3N_4.

3.3. Optical properties

The UV–vis diffuse reflection spectra (UV–vis DRS) were used to investigate the optical properties of the photocatalysts. The UV–vis diffuse reflectance spectroscopy of photocatalysts is shown in Fig. 7(a). The g-C_3N_4 displayed a strong absorption within the visible-light range, indicating its potential for visible-light harvesting. The absorption edge of the g-C_3N_4@HNTs was observed at

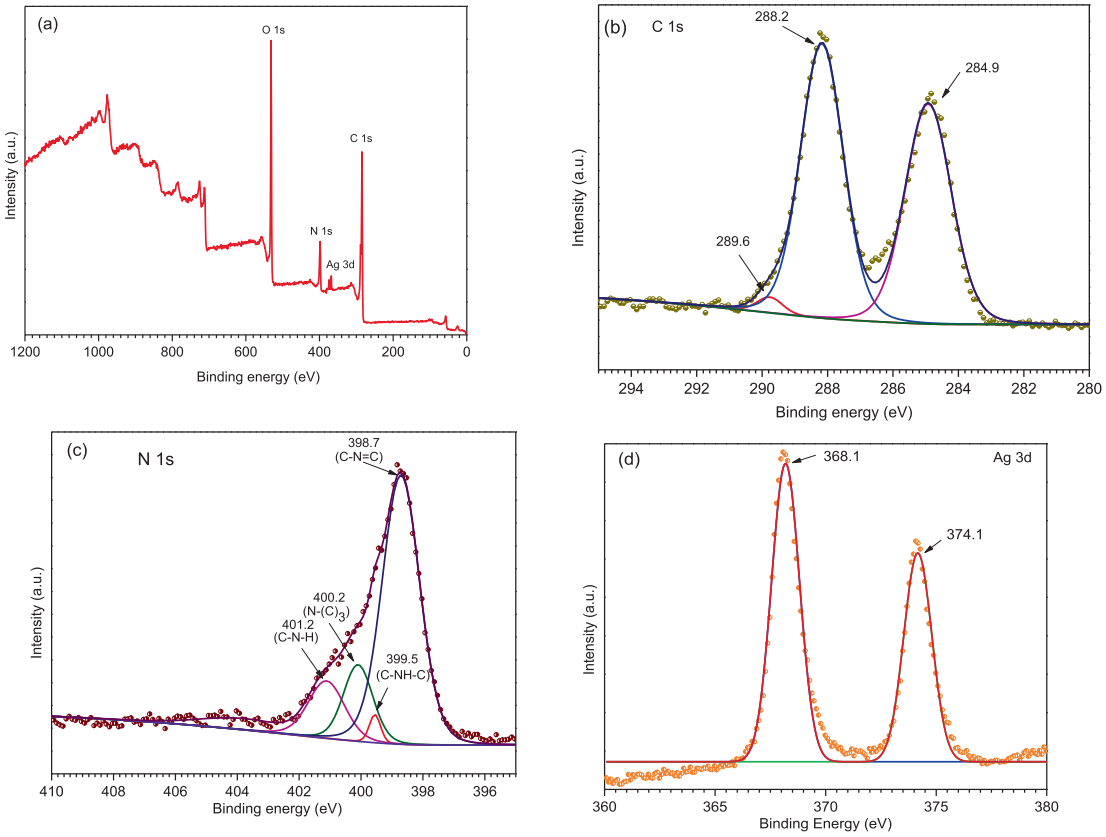

Fig. 3. XPS (a) survey scan, (b) C1s, (c) N1s, and (d) Ag3d spectra of Ag-g-C_3N_4@HNTs nanocomposite.

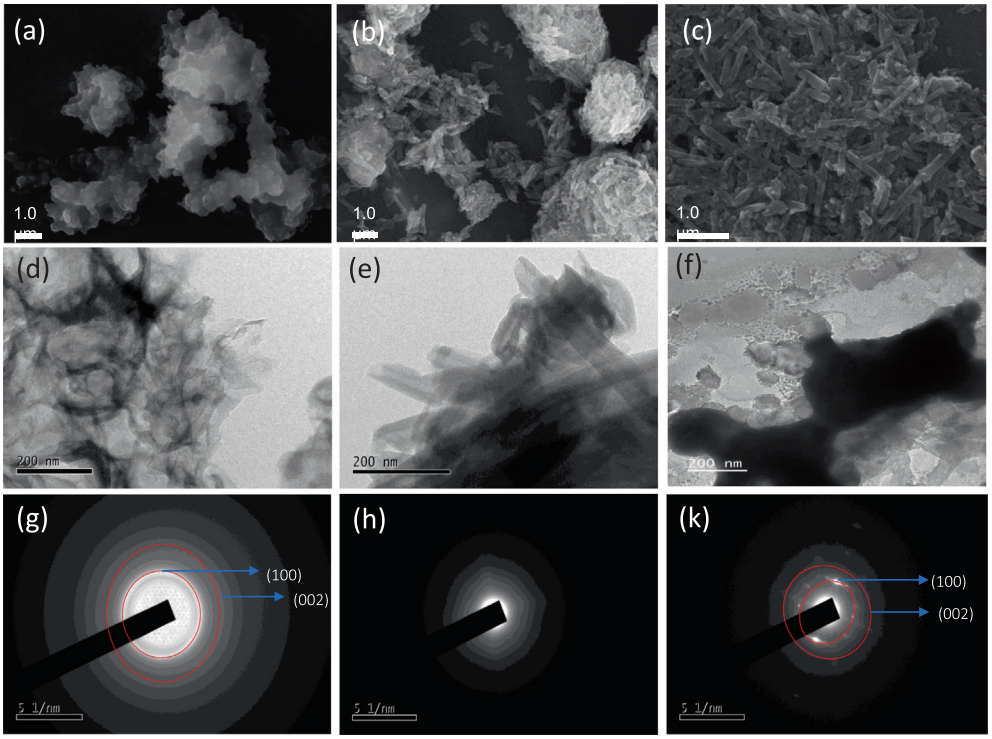

Fig. 4. SEM images of (a) g-C_3N_4, (b) Halloysite, (c) Ag-g-C_3N_4@HNTs nanocomposite; TEM images of (d) g-C_3N_4, (e) Halloysite, (f) Ag-g-C_3N_4@HNTs nanocomposite; SAED spectra of (g) g-C_3N_4, (h) Halloysite, (k) Ag-g-C_3N_4@HNTs nanocomposite.

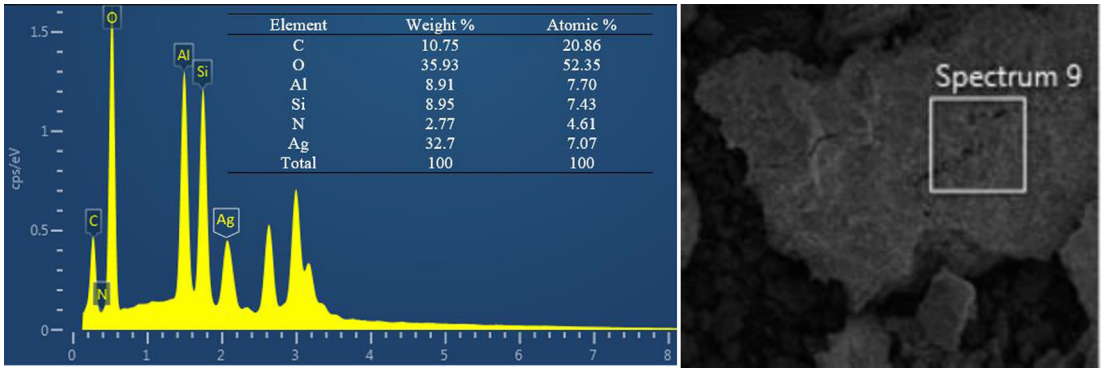

Fig. 5. EDX pattern of Ag-g-C_3N_4@HNTs nanocomposite.

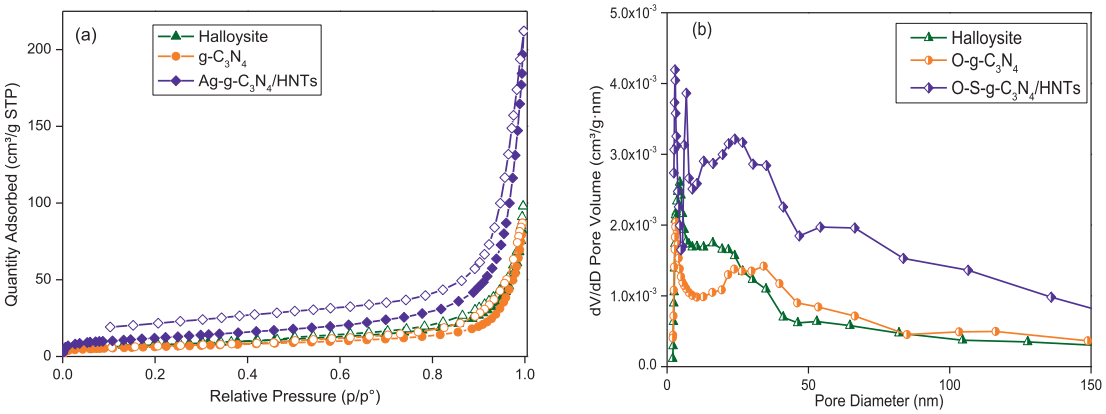

Fig. 6. (a) N_2 adsorption–desorption isotherms and (b) Pore size distribution of HNTs, g-C_3N_4, and Ag-g-C_3N_4@HNTs nanocomposite.

Table 1
BET specific surface (S_{BET}), pore volume (Vp), and pore size (D) of HNTs, Ag-g-C_3N_4, and Ag-g-C_3N_4@HNTs nanocomposite.

Samples	SBET (m^2/g)	Vp (cm^3 g^{-1})	D (mm)[a]
HNTs	28.01	0.137	19.67
g-C3N4	20.12	0.107	20.34
Ag-g-C_3N_4@HNTs	43.04	0.273	28.14

around 490 nm, which is consistent with the intrinsic bandgap of g-C_3N_4. The Ag-g-C_3N_4@HNTs catalyst displayed strong adsorption at about 510 nm characterization of silver surface plasmon resonance of Ag-NPs. The above results demonstrated that Ag particles play an important role in enhancing photocatalytic activity. Furthermore, the hollow tube structure of the halloysite contributed to increased light absorption ability. Therefore, the enhanced visible-light absorption of the Ag-g-C_3N_4@HNTs nanocomposite was proposed because of the resonance effect between Ag-g-C_3N_4 and halloysite materials. The bandgap (*Eg*) of the samples can be calculated from the following Equation (2):

$$\alpha h\upsilon = A(h\upsilon - Eg)^{n/2} \quad (2)$$

where *Eg,* is the bandgap energy of the semiconductor, *A* is the adsorption constant, *h* is Planck's constant, α and v represent the absorption coefficient and the light frequency, respectively, and *n* is 1 for the direct transition. The bandgap energy of g-C_3N_4, g-C_3N_4@HNTs, and Ag-g-C_3N_4@HNTs samples, therefore, have been calculated corresponding Tauc plots of the $(\alpha hv)^{1/2}$ versus photon energy (hv), which shows *Eg,* values of 2.7 eV, 2.6 eV, 2.5 eV.

The charge separation of catalysts was investigated using photoluminescence (PL) spectra analysis at room temperature. The separation and migration processes of photogenerated charge carriers are revealed using PL [50]. PL spectra of g-C_3N_4, g-C_3N_4@HNTs, and Ag-g-C_3N_4@HNTs are shown in Fig. 7(b). It is observed that g-C_3N_4, g-C_3N_4@HNTs, and Ag-g-C_3N_4@HNTs show a similar broad emission peak at around 430 nm. A decrease in the PL intensity of the composite can be observed compared with pure g-C_3N_4. The weaker peak intensity indicates that AgNPs on the surface of g-C_3N_4 sheets can inhibit the recombination of photogenerated charge carriers, implying that efficient separation of photoexcited charge carriers is beneficial to enhancing the photocatalytic activity and performance yield.

As indicated in Fig. 7(c), the photocurrent density of the g-C_3N_4 and g-C_3N_4@HNTs decreases following an increase in time. Under the same conditions, however, the photocurrent density of the Ag-g-C_3N_4@HNTs nanocomposite is significantly higher. This result is suitable with the PL spectra; the excited electrons and holes of g-C_3N_4 were efficiently separated due to electrostatic interaction between g-C_3N_4 and the negatively charged halloysite surface [51].

Electron paramagnetic resonance (EPR) was used to study the unpaired electron in the samples. Fig. 7(d) shows the EPR of g-C_3N_4 and Ag-g-C_3N_4@HNTs nanocomposite. The conduction electrons in the localized π-states of g-C_3N_4 are attributed to g = 2.003 in the samples [52]. As can be seen, the signal strength of Ag-g-C_3N_4@HNTs is lower than pure g-C_3N_4, implying that the density of internal hydrogen decreased due to the decrease in lone pair electrons [53].

3.4. Photocatalytic properties

As shown in Fig. 8(a), the halloysite removed approximately 36% of TC within four hours, probably because of the adsorption

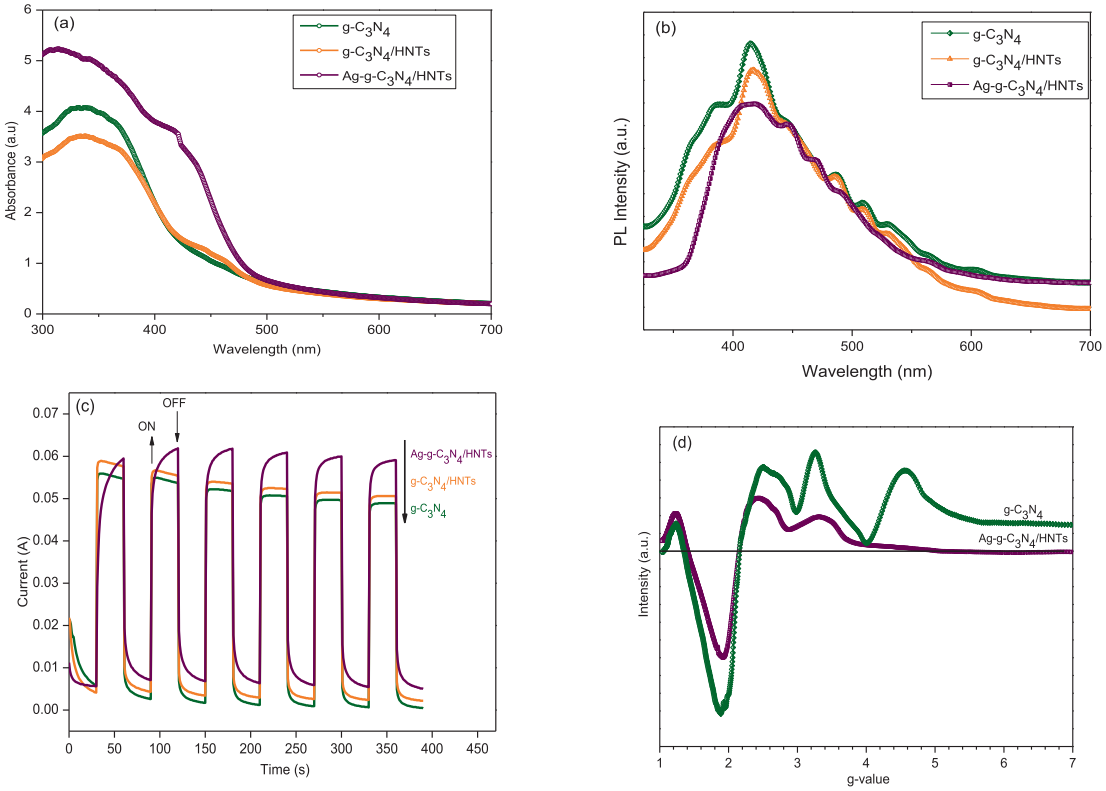

Fig. 7. (a) UV–vis diffuse reflectance spectra, (b) photoluminescence spectra, and (c) transient photocurrent response of g-C_3N_4, g-C_3N_4@HNTs, and Ag-g-C_3N_4@HNTs nanocomposite,(d) EPR spectra of g-C_3N_4 and Ag-g-C_3N_4@HNTs nanocomposite.

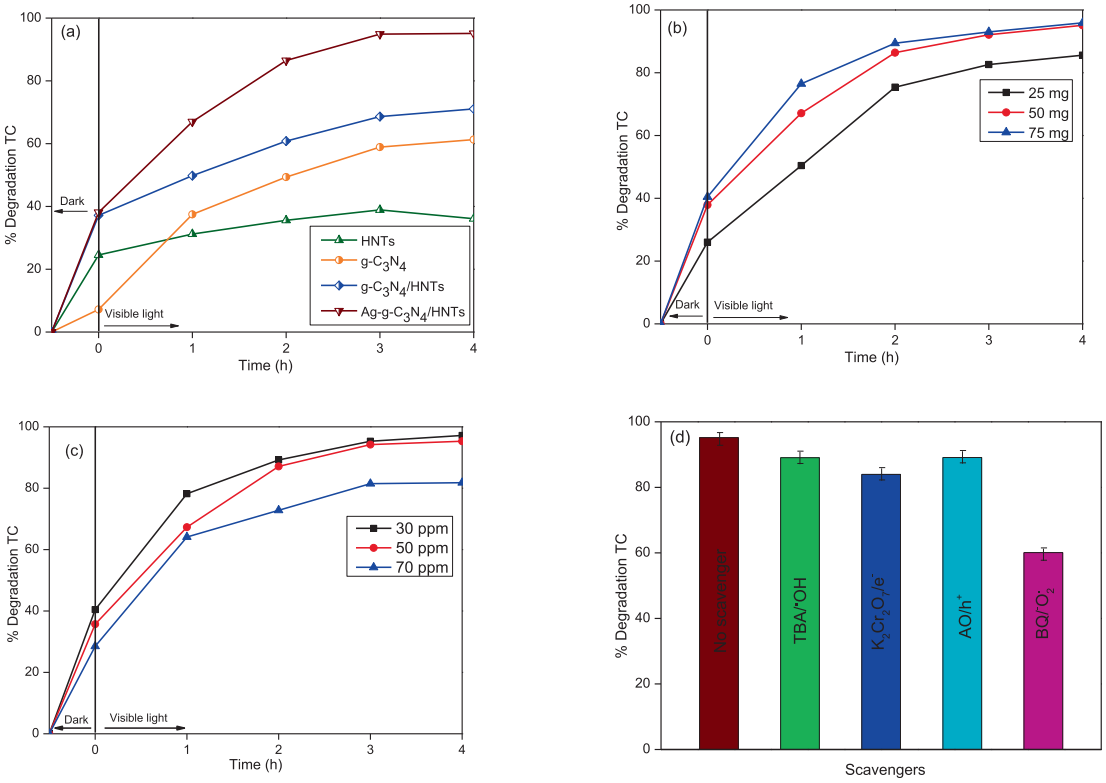

Fig. 8. Photodegradation of TC under various conditions of (a) photocatalysts, (b) photocatalyst dosage, (c) concentration of TC, (d) active species trapping experiments for degradation of TC over Ag-g-C_3N_4@HNTs nanocomposite.

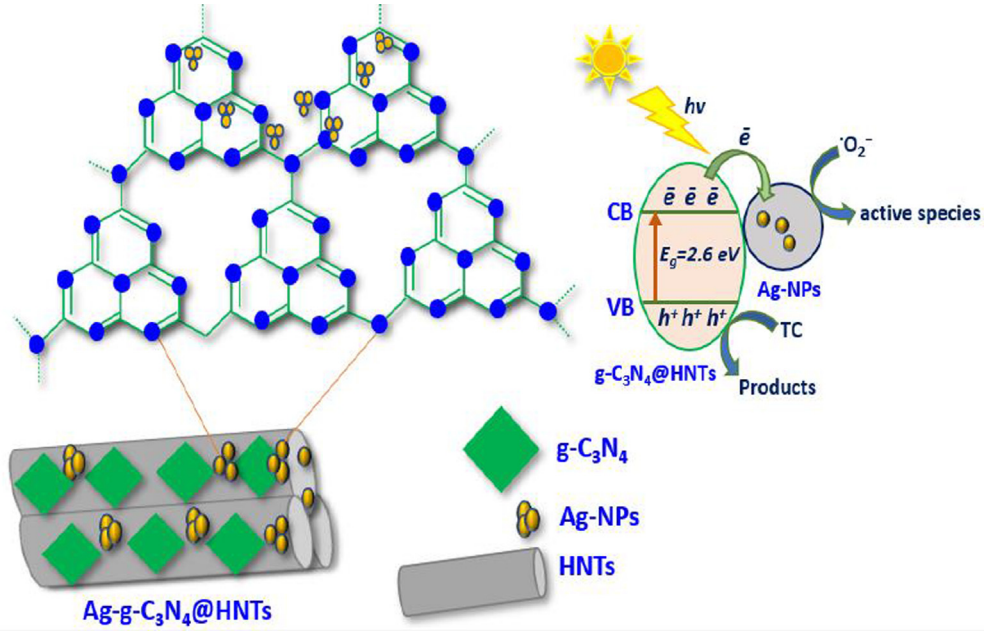

Fig. 9. Schematic illustration of active species in the photodegradation of TC by Ag-g-C_3N_4@HNTs under visible light irradiation.

ability of the halloysite. This result could prompt speculation that TC is a positively charged organic substrate attracted by the negatively charged external surface of the HNTs tubes [54]. At the same time, after four hours under visible-light irradiation, about 61% TC was degraded with g-C_3N_4 material, which could be related to the fast recombination of photogenerated electrons and holes and limited surface area, which limits the photocatalytic capacity of the g-C_3N_4 [52]. The g-C_3N_4@HNTs and Ag-g-C_3N_4@HNTs nanocomposite exhibited 71% and 95% TC was degraded in four hours, respectively. Thus, the photocatalytic activity of Ag-g-C_3N_4@HNTs nanocomposites is higher than g-C_3N_4@HNTs. This may be due to the high surface area of Ag-g-C_3N_4@HNTs resulting in improved photocatalytic degradation efficiency because more electron-hole pairs could be excited under the same light irradiation conditions, and the surface plasmon resonance of Ag-NPs can generate hot electrons and hot holes, which can prompt and improve surface chemical reactions [55]. In addition, the negatively charged external surface of the HNTs formed electrostatic interactions with the TC molecules, reducing the recombination of the photogenerated electron-hole pair recombination in g-C_3N_4.

3.4.1. Effect of photocatalyst dosage

The effect of photocatalyst dosage on the photodegradation of TC was investigated by varying Ag-g-C_3N_4@HNTs photocatalyst dosage. As shown in Fig. 8(b), photodegradation of TC increased from 85.4% to 95.9% with increasing photocatalyst dosage from 25 mg to 75 mg, respectively. Notably, the difference in TC degradation efficiency between 50 mg and 75 mg of the photocatalyst was insignificant. The increased photodegraded efficiency with 50 mg catalyst could be attributed to increased photocatalyst active sites and the production of free electrons in the conduction band. Paola Semeraro et al. [56] reported a similar result, claiming that when the catalytic dosage went up from 10 mg to 15 mg, a slight increase in TC degradation efficiency was initially observed. However, after 150 min of irradiation, no further rise of TC degradation occurred, most likely due to the lack of tetracycline molecules. Consequently, 50 mg of Ag-g-C_3N_4@HNTs nanocomposite was used for TC degradation in subsequent experiments.

3.4.2. Effect of TC concentration

Photocatalytic degradation of TC over Ag-g-C_3N_4@HNTs catalyst was studied by varying the initial TC concentration while maintaining a constant photocatalyst dosage (50 mg). Fig. 8(c) shows that the photodegradation efficiency declined from 97.1% to 81.6% as the initial TC concentration increased from 30 ppm to 70 ppm. According to the theory, more TC molecules could be adsorbed on the catalyst surface when the initial TC concentration rises. Because the catalyst surface has fewer free sites for receiving photons, a substantial amount of adsorbed TC and its intermediates in the degradation process may inhibit further photocatalytic degradation of TC.

3.4.3. Active species trapping experiments

Trapping experiments of the active species of TC degradation were carried out to understand the photocatalytic process. As shown in Fig. 8(d), the photocatalytic degradation of TC with *tert*-Butyl alcohol (TBA, scavenger of $^{\bullet}OH$) and ammonium oxalate monohydrate (AO, scavenger of h^+) has an insignificant difference from that with no scavenger, implying that $^{\bullet}OH$ and h^+ are not the main active species. With potassium dichromate ($K_2Cr_2O_7$, scavenger of e^-), the TC degradation slowed down and stopped at 84%, implying that the photogenerated electron plays a minor role in the photocatalyst. In comparison, when 1.4-benzoquinone (BQ, scavenger of $^{\bullet}O_2^-$) is added, the TC degradation efficiency is reduced to 60%, suggesting that $^{\bullet}O_2^-$ was the primary active species and played a critical role in the photocatalyst. Thus, $^{\bullet}O_2^-$ is the crucial oxidative species for the degradation of TC, as it is produced by the reaction of photogenerated electrons with O_2 in water. Charge transfer from the conducting band of Ag-C_3N_4@HNTs to Ag nanoparticles as depicted in Fig. 9.

According to the above results, $^{\bullet}O_2^-$ plays a significant role in the degradation of TC and the mechanism of TC decomposition could have been proposed in Fig. 10. Firstly, TC molecules ($C_{22}H_{25}N_2O_8$, m/z = 444) are directly oxidized, resulting in the loss of the *N*-dimethyl group and ring-opening process to form a compound with a molecular mass of 332. The product (m/z = 332) is then decomposed to $C_{16}H_{15}O_7$ (m/z = 316) via a further oxidized

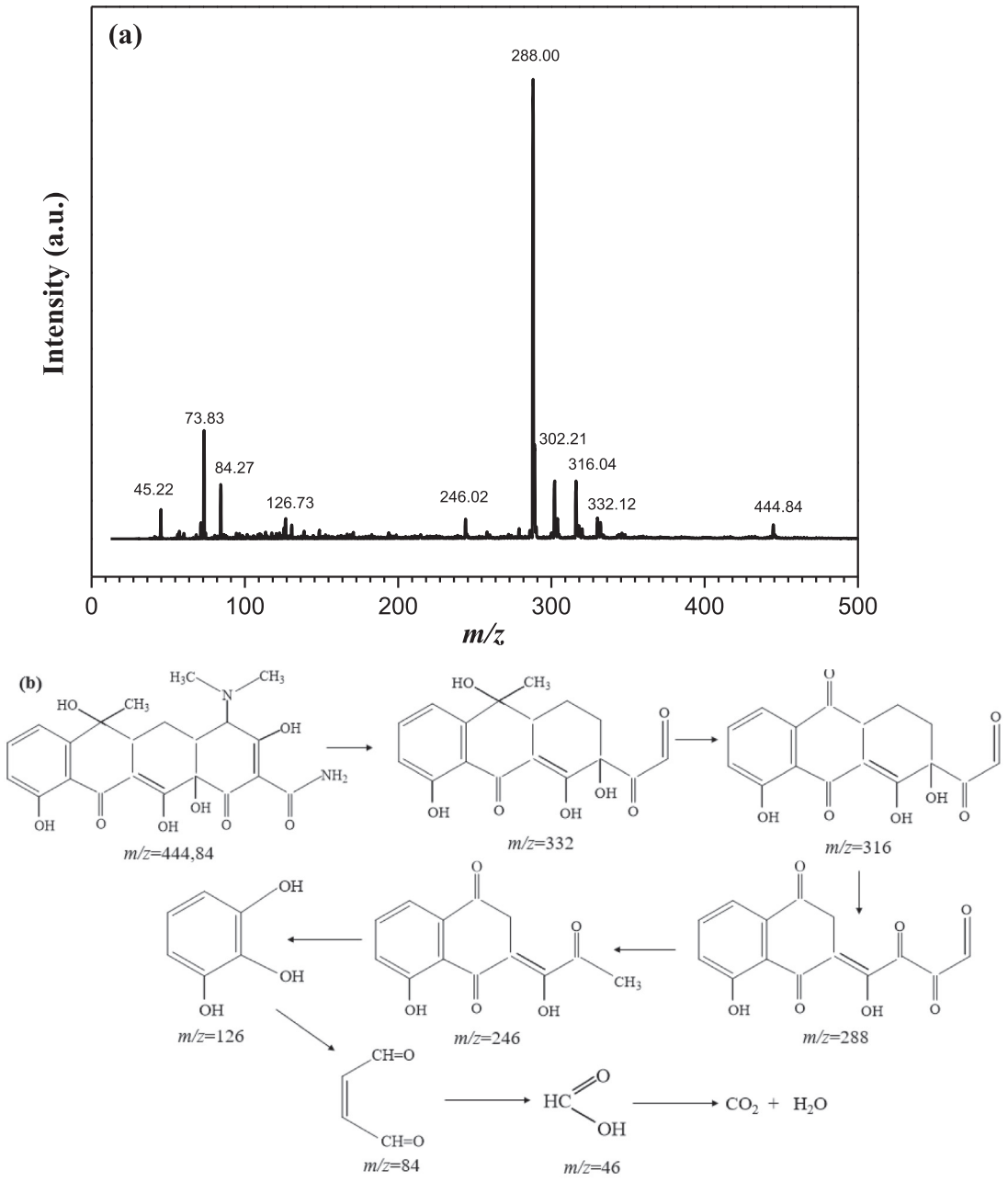

Fig. 10. HPLC-MS analysis of the intermediate product (a) and the possible pathway (b) of the TC photodegradation over Ag@g-C_3N_4/HNTs.

Table 2
Comparative photocatalytic efficiency of various catalysts used for the removal of TC.

Catalyst	Degradation (%)	Experimental conditions				Reference
		Concentration (mg/L)	Volume (mL)	Time (h)	Dosage (mg)	
$Mn_3Gd_{7-x}Ce_x(SiO_4)_6O_{1.5}$	99.8	400	200	0.5	400	[58]
g-US-1	83	20	100	3	50	[59]
5%wt- NMIL/BWO	77.78	20	100	2	40	[60]
Ag/PCN-3	84	20	30	2	50	[57]
Ag-g-C_3N_4@HNTs	95	50	30	4	50	This work

reaction. The intermediate compounds with smaller mass (m/z = 302, 288, 246, 126, 84 and 46) by ring cleavage with the oxidation process. Finally, these intermediates are gradually mineralized to form CO_2 and H_2O.

Table 2 summarises the photodegradation efficiency of the various catalysts for TC molecules. According to the existing literature, TC degradation has been performed by various types of catalysts under different conditions. The photocatalytic efficiency of the

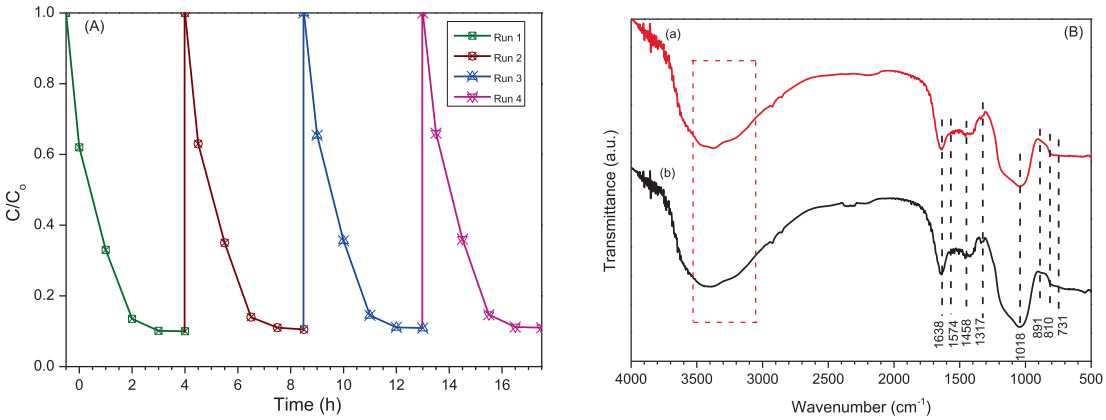

Fig. 11. (a) Cycling runs for the photodegradation of TC over the Ag-g-C_3N_4@HNTs nanocomposite, (b) FT-IR spectra of fresh Ag-g-C_3N_4@HNTs nanocomposites and used Ag-g-C_3N_4@HNTs nanocomposites.

Ag-g-C_3N_4@HNTs nanocomposite is higher than that found in previous studies. Hence, the Ag-g-C_3N_4@HNTs nanocomposite can be considered an excellent photocatalyst in applications for organic decomposition.

3.5. Catalytic stability

The stability of a photocatalyst is a crucial issue for industrial applications. The photocatalytic capability of Ag-g-C_3N_4@HNTs nanocomposite was assessed in four successive runs, and its performance is shown in Fig. 11(a). The photocatalytic degradation efficiency still reached 91% after the four cycles. In addition, the FT-IR spectra of the recycled Ag-g-C_3N_4@HNTs nanocomposite showed that the characteristic absorption peaks of Ag-g-C_3N_4@HNTs remained unchanged from those of the fresh sample (Fig. 11(b)). The catalyst had high stability during photoreaction and excellent photostability up to four cycles.

4. Conclusions

In summary, the novel Ag-g-C_3N_4@HNTs nanocomposite was successfully synthesized through a green method. The improved photocatalytic efficiency of the nanocomposite was a result of the following various factors: the large surface area, the surface plasmon resonance of Ag-NPs, and the negatively charged external surface of the HNTs. The nanocomposite exhibited excellent photocatalytic performance for TC degradation. Typically, the TC degradation reached 95% after four hours under visible light with only a minor decrease in efficiency after four recycles. It is expected that this work will provide a new and low-cost composite material as an active and durable photocatalyst in water treatment.

Declaration of Competing Interest

The authors declare that they have no known competing financial interests or personal relationships that could have appeared to influence the work reported in this paper.

Acknowledgments

HTN thanks support from the Vingroup Joint Stock Company through the Domestic Master/PhD Scholarship Programme of Vingroup Innovation Foundation (VINIF), code VINIF.2021.ThS.83. HVD thanks the Royal Society of Chemistry for the Research Fund Grant (R20-8172) and the UK Engineering and Physical Sciences Research Council for the EPSRC Doctoral Prize Fellowship (EP/T517872/1).

References

[1] M. Palaniappan, P. Gleick, L. Allen, M. Cohen, J.C. Smith, C. Smith, Clearing the waters: a focus on water quality solutions, 2010.
[2] K. Rajeshwar, M.E. Osugi, W. Chanmanee, C.R. Chenthamarakshan, M.V.B. Zanoni, P. Kajitvichyanukul, R. Krishnan-Ayer, Heterogeneous photocatalytic treatment of organic dyes in air and aqueous media, J. Photochem. Photobiol. C Photochem. Rev. 9 (2008) 171–192.
[3] Z. Wei, J. Liu, W. Shangguan, A review on photocatalysis in antibiotic wastewater: Pollutant degradation and hydrogen production, Chinese, J. Catal. 41 (2020) 1440–1450.
[4] A. Koltsakidou, Z. Terzopoulou, G.Z. Kyzas, D.N. Bikiaris, D.A. Lambropoulou, Biobased poly (ethylene furanoate) polyester/TiO2 supported nanocomposites as effective photocatalysts for anti-inflammatory/analgesic drugs, Molecules 24 (2019) 564.
[5] N. Daneshvar, D. Salari, A. Niaei, A.R. Khataee, Photocatalytic degradation of the herbicide erioglaucine in the presence of nanosized titanium dioxide: comparison and modeling of reaction kinetics, J. Environ. Sci. Heal. Part B. 41 (2006) 1273–1290.
[6] E.W. Chu, J.R. Karr, Environmental impact: Concept, consequences, measurement, Ref. Modul. Life Sci. (2017).
[7] N. López-Salas, M. Antonietti, Carbonaceous Materials: The Beauty of Simplicity, Bull. Chem. Soc. Jpn. 94 (2021) 2822–2828.
[8] S. Kumar, G. Saeed, L. Zhu, K.N. Hui, N.H. Kim, J.H. Lee, 0D to 3D carbon-based networks combined with pseudocapacitive electrode material for high energy density supercapacitor: A review, Che. Eng. J. 403 (2021).
[9] J. Wang, H. Kong, J. Zhang, Y. Hao, Z. Shao, F. Ciucci, Carbon-based electrocatalysts for sustainable energy applications, Pro. Mater. Sci. 116 (2021).
[10] M. SaidulIslam, Y. Shudo, S. Hayami, Energy Conversion and Storagein Fuel Cells and Super-Capacitors from Chemical Modifications of Carbon Allotropes: State-of-Art and Prospect, Bull. Chem. Soc. Jpn. 95 (2022) 1–25.
[11] S. Pany, K.M. Parida, A facile in situ approach to fabricate N, S-TiO_2/gC_3N_4 nanocomposite with excellent activity for visible light induced water splitting for hydrogen evolution, Phys Chem Chem. Phys. 17 (2015) 8070–8077.
[12] J. Tian, Q. Liu, A.M. Asiri, X. Sun, Y. He, Ultrathin graphitic C_3N_4 nanofibers: hydrolysis-driven top-down rapid synthesis and application as a novel fluorosensor for rapid, sensitive, and selective detection of Fe^{3+}, Sensors Actuators B Chem. 216 (2015) 453–460.
[13] Q. Chen, Y. Zhao, X. Huang, N. Chen, L. Qu, Three-dimensional graphitic carbon nitride functionalized graphene-based high-performance supercapacitors, J. Mater. Chem. A 3 (2015) 6761–6766.
[14] Y. Oh, V.D. Le, U.N. Maiti, J.O. Hwang, W.J. Park, J. Lim, K.E. Lee, Y. Bae, Y. Kim, S. O. Kim, Selective and regenerative carbon dioxide capture by highly polarizing porous carbon nitride, ACS Nano. 9 (2015) 9148–9157.
[15] Q. Yang, W. Wang, Y. Zhao, J. Zhu, Y. Zhu, L. Wang, Metal-free mesoporous carbon nitride catalyze the Friedel-Crafts reaction by activation of benzene, RSC Adv. 5 (2015) 54978–54984.
[16] S. Ma, S. Zhan, Y. Jia, Q. Shi, Q. Zhou, Enhanced disinfection application of Ag-modified g-C_3N_4 composite under visible light, Appl. Catal. B Environ. 186 (2016) 77–87.
[17] R. Chen, J. Zhang, Y. Wang, X. Chen, J.A. Zapien, C.S. Lee, Graphitic carbon nitride nanosheet@metal-organic framework core-shell nanoparticles for photo-chemo combination therapy, Nanoscale 7 (2015) 17299–17305.
[18] X. Zhou, F. Peng, H. Wang, H. Yu, Y. Fang, Carbon nitride polymer sensitized TiO_2 nanotube arrays with enhanced visible light photoelectrochemical and photocatalytic performance, Chem. Commun 47 (2011) 10323–10325.

[19] D.A. Tran, C.T.N. Pham, T.N. Ngoc, H.N. Phi, Q.T.H. Ta, D.H. Truong, V.T. Nguyen, H.H. Luc, L.T. Nguyen, N.N. Dao, S.J. Kim, V. Vo, One-step synthesis of oxygen doped g-C_3N_4 for enhanced visible-light photodegradation of Rhodamine B, J. Phys. Chem. Solids 151 (2021).

[20] Y. Song, J. Qi, J. Tian, S. Gao, F. Cui, Construction of Ag/g-C_3N_4 photocatalysts with visible-light photocatalytic activity for sulfamethoxazole degradation, Chem. Eng. J. 341 (2018) 547–555.

[21] S. Samanta, S. Martha, K. Parida, Facile synthesis of Au/g-C_3N_4 nanocomposites: an inorganic/organic hybrid plasmonic photocatalyst with enhanced hydrogen gas evolution under visible-light irradiation, Chem. Cat. Chem. 6 (2014) 1453–1462.

[22] J. Ding, X. Sun, Q. Wang, D. Li, X. Li, X. Li, L. Chen, X. Zhang, X. Tian, K. Ostrikov, Plasma synthesis of Pt/g-C_3N_4 photocatalysts with enhanced photocatalytic hydrogen generation, J. Alloys Compd. 873 (2021).

[23] D. Hao, J. Ren, Y. Wang, H. Arandiyan, M. Garbrecht, X. Bai, H.K. Shon, W. Wei, B. Ni, A green synthesis of Ru modified g-C_3N_4 nanosheets for enhanced photocatalytic ammonia synthesis, Energy Mater. Adv. 2021 (2021).

[24] J. Wang, J. Cong, H. Xu, J. Wang, H. Liu, M. Liang, J. Gao, Q. Ni, J. Yao, Facile gel-based morphological control of Ag/g-C_3N_4 porous nanofibers for photocatalytic hydrogen generation, ACS Sustain. Chem. Eng. 5 (2017) 10633–10639.

[25] Y. Bu, Z. Chen, W. Li, Using electrochemical methods to study the promotion mechanism of the photoelectric conversion performance of Ag-modified mesoporous g-C_3N_4 heterojunction material, Appl. Catal. B Environ. 144 (2014) 622–630.

[26] Y. Li, J. Zhan, L. Huang, H. Xu, H. Li, R. Zhang, S. Wu, Synthesis and photocatalytic activity of a bentonite/gC_3N_4 composite, Rsc. Adv. 4 (2014) 11831–11839.

[27] M.B. Nguyen, X.N. Pham, H.V. Doan, Heterostructure of vanadium pentoxide and mesoporous SBA-15 derived from natural halloysite for highly efficient photocatalytic oxidative desulphurisation, RSC Adv. 11 (2021) 31738–31745.

[28] H. Zhang, Selective modification of inner surface of halloysite nanotubes: A review, Nanotechnol. Rev. 6 (2017) 573–581.

[29] M. Darvishnejad, H. Ebrahimzadeh, Graphitic carbon nitride-reinforced polymer ionic liquid nanocomposite: a novel mixed-mode sorbent for microextraction in packed syringe, Int. J. Environ. Anal. Chem. 1–14 (2020).

[30] L. Wang, W. Zhang, Y. Su, Z. Liu, C. Du, Halloysite derived 1D mesoporous tubular g-C_3N_4: Synergy of template effect and associated carbon for boosting photocatalytic performance toward tetracycline removal, Appl. Clay. Sci. 213 (2021).

[31] X.N. Pham, M.B. Nguyen, H.V. Doan, Direct synthesis of highly ordered Ti-containing Al-SBA-15 mesostructured catalysts from natural halloysite and its photocatalytic activity for oxidative desulfurization of dibenzothiophene, Adv. Powder Technol. 31 (2020) 3351–3360.

[32] X.N. Pham, H.T. Nguyen, N.T. Pham, Green synthesis and antibacterial activity of HAp@ Ag nanocomposite using Centella asiatica (L.) Urban extract and eggshell, Int. J. Biomater. 2020 (2020).

[33] S. Cao, J. Low, J. Yu, M. Jaroniec, Polymeric Photocatalysts Based on Graphitic Carbon Nitride, Adv. Mater. 27 (2015) 2150–2176.

[34] X. Wang, K. Maeda, A. Thomas, K. Takanabe, G. Xin, J.M. Carlsson, K. Domen, M. Antonietti, A metal-free polymeric photocatalyst for hydrogen production from water under visible light, Nat. Mater. 8 (2009) 76–80.

[35] R. Kamble, M. Ghag, G. Gaikawad, B.K. Panda, Halloysite Nanotubes and Applications: A Review, J. Adv. Sci. Res. 3 (2012).

[36] S.R. Levis, P.B. Deasy, Characterisation of halloysite for use as a microtubular drug delivery system, Int. J. Pharm. 243 (2002) 125–134.

[37] S. Zeng, C. Reyes, J. Liu, P.A. Rodgers, S.H. Wentworth, L. Sun, Facile hydroxylation of halloysite nanotubes for epoxy nanocomposite applications, Polymer (Guildf) 55 (2014) 6519–6528.

[38] A. Baghizadeh, S. Ranjbar, V.K. Gupta, M. Asif, S. Pourseyedi, M.J. Karimi, R. Mohammadinejad, Green synthesis of silver nanoparticles using seed extract of Calendula officinalis in liquid phase, J. Mol. Liq. 207 (2015) 159–163.

[39] L. Wang, J. Chen, L. Ge, Z. Zhu, V. Rudolph, Halloysite-nanotube-supported Ru nanoparticles for ammonia catalytic decomposition to produce COx-free hydrogen, Energy & Fuels 25 (2011) 3408–3416.

[40] H. Huang, K. Xiao, N. Tian, F. Dong, T. Zhang, X. Du, Y. Zhang, Template-free precursor-surface-etching route to porous, thin gC_3N_4 nanosheets for enhancing photocatalytic reduction and oxidation activity, J. Mater. Chem. A 5 (33) (2017) 17452–17463.

[41] Y. Sun, W. Zhang, T. Xiong, Z. Zhao, F. Dong, R. Wang, W. Ho, Growth of BiOBr nanosheets on C_3N_4 nanosheets to construct two-dimensional nanojunctions with enhanced photoreactivity for NO removal, J. Colloid Interface Sci. 418 (2014) 317–323.

[42] P. Senthil Kumar, S. Sobiya, M. Selvakumar, S. Ganesh Babu, S. Karuthapandian, Hierarchically structured CuO/g-C_3N_4 heterogeneous semiconductor photocatalyst with improved photocatalytic activity and stability, Energy Environ. Focus 5 (2016) 139–149.

[43] Y.P. Zhu, T.Z. Ren, Z.Y. Yuan, Mesoporous phosphorus-doped g-C_3N_4 nanostructured flowers with superior photocatalytic hydrogen evolution performance, ACS Appl. Mater. Interfaces 7 (2015) 16850–16856.

[44] F. Wei, Y. Liu, H. Zhao, X. Ren, J. Liu, T. Hasan, L. Chen, Y. Li, B.L. Su, Oxygen self-doped gC_3N_4 with tunable electronic band structure for unprecedentedly enhanced photocatalytic performance, Nanoscale 10 (2018) 4515–4522.

[45] T. Yeh, C. Teng, S. Chen, H. Teng, Nitrogen-doped graphene oxide quantum dots as photocatalysts for overall water-splitting under visible light Illumination, Adv. Mater. 26 (2014) 3297–13203.

[46] H.V. Doan, H.T. Nguyen, V.P. Ting, S. Guan, J.C. Eloi, S.R. Hall, X.N. Pham, Improved photodegradation of anionic dyes using a complex graphitic carbon nitride and iron-based metal-organic framework material, Faraday Discuss. 231 (2021) 81–96.

[47] S.W. Cao, Y.P. Yuan, J. Barber, S.C.J. Loo, C. Xue, Noble-metal-free g-C_3N_4/Ni$(dmgH)_2$ composite for efficient photocatalytic hydrogen evolution under visible light irradiation, Appl. Surf. Sci. 319 (2014) 344–349.

[48] L. Ge, C. Han, J. Liu, Y. Li, Enhanced visible light photocatalytic activity of novel polymeric gC_3N_4 loaded with Ag nanoparticles, Appl. Catal. A Gen. 409 (2011) 215–222.

[49] Y.M. Lvov, D.G. Shchukin, H. Mohwald, R.R. Price, Halloysite clay nanotubes for controlled release of protective agents, ACS Nano. 2 (2008) 814–820.

[50] L. Lin, H. Ou, Y. Zhang, X. Wang, Tri-s-triazine-based crystalline graphitic carbon nitrides for highly efficient hydrogen evolution photocatalysis, Acs. Catal. 6 (2016) 3921–3931.

[51] K.C. Christoforidis, M. Melchionna, T. Montini, D. Papoulis, E. Stathatos, S. Zafeiratos, E. Kordouli, P. Fornasiero, Solar and visible light photocatalytic enhancement of halloysite nanotubes/gC_3N_4 heteroarchitectures, RSC Adv. 89 (2016) 86617–86626.

[52] W. Ho, Z. Zhang, M. Xu, X. Zhang, X. Wang, Y. Huang, Enhanced visible-light-driven photocatalytic removal of NO: Effect on layer distortion on g-C_3N_4 by H_2 heating, Appl. Catal. B Environ. 179 (2015) 106–112.

[53] J. Wang, Z. Yang, W. Yao, X. Gao, D. Tao, Defects modified in the exfoliation of g-C_3N_4 nanosheets via a self-assembly process for improved hydrogen evolution performance, Appl. Catal. B Environ. 238 (2018) 629–637.

[54] D. Papoulis, Halloysite based nanocomposites and photocatalysis: a review, Appl. Clay. Sci. 168 (2019) 164–174.

[55] D.Y. Wu, M. Zhang, L.B. Zhao, Y.F. Huang, B. Ren, Z.Q. Tian, Surface plasmon-enhanced photochemical reactions on noble metal nanostructures, Sci. China Chem. 58 (2015) 574–585.

[56] P. Semeraro, S. Bettini, S. Sawalha, S. Pal, A. Licciulli, F. Marzo, N. Lovergine, L. Valli, G. Giancane, Photocatalytic degradation of tetracycline by ZnO/γ-Fe_2O_3 paramagnetic nanocomposite material, Nanomaterials 10 (2020) 1458.

[57] W. Xu, S. Lai, S.C. Pillai, W. Chu, Y. Hu, X. Jiang, M. Fu, X. Wu, F. Li, H. Wang, Visible light photocatalytic degradation of tetracycline with porous Ag/graphite carbon nitride plasmonic composite: degradation pathways and mechanism, J. Colloid Interface Sci. 574 (2020) 110–121.

[58] J. Fu, N. Liu, L. Mei, L. Liao, D. Deyneko, J. Wang, Y. Bai, G. Lv, Synthesis of Ce-doped $Mn_3Gd_{7x}Ce_x(SiO_4)_6O_{1.5}$ for the enhanced catalytic ozonation of tetracycline, Sci. Rep. 9 (2019) 1–10.

[59] H. Zhang, J. Li, X. He, B. Liu, Preparation of a g-C_3N_4/UiO-66-NH_2/CdS Photocatalyst with Enhanced Visible Light Photocatalytic Activity for Tetracycline Degradation, Nanomaterials 19 (2020) 1824.

[60] S. Yin, Y. Chen, Q. Hu, M. Li, Y. Ding, J. Di, J. Xia, H. Li, Construction of NH_2-MIL-125(Ti) nanoplates modified Bi_2WO_6 microspheres with boosted visible-light photocatalytic activity, Res. Chem. Intermed. 46 (2020) 3311–3326.